

# Utility of Hovmöller diagrams to diagnose Rossby wave trains

By ILONA GLATT<sup>1\*</sup>, ANDREAS DÖRNBRACK<sup>2</sup>, SARAH JONES<sup>3</sup>, JULIA KELLER<sup>3</sup>, O. MARTIUS<sup>4</sup>, AURELIA MÜLLER<sup>3</sup>, DIETER H. W. PETERS<sup>5</sup> and VOLKMAR WIRTH<sup>1</sup>,  
<sup>1</sup>*Institut für Physik der Atmosphäre, Johannes Gutenberg-Universität Mainz, Mainz, Germany;* <sup>2</sup>*Institut für Physik der Atmosphäre, Deutsches Zentrum für Luft- und Raumfahrt, Oberpfaffenhofen, Germany;* <sup>3</sup>*Karlsruher Institut für Technologie, Institut für Meteorologie und Klimaforschung (IMK-TRO), Karlsruhe, Germany;* <sup>4</sup>*Institute of Geography, University of Bern, Oeschger Centre for Climate Change Research, Bern, Switzerland;* <sup>5</sup>*Leibniz-Institut für Atmosphärenphysik e.V., Universität Rostock, Kühlungsborn, Germany*

(Manuscript received 23 December 2010; in final form 12 July 2011)

## ABSTRACT

The study investigates and compares various methods that aim to diagnose Rossby wave trains with the help of Hovmöller diagrams. Three groups of methods are distinguished: The first group contains trough-and-ridge Hovmöller diagrams of the meridional wind; they provide full phase information, but differ in the method for latitudinal averaging or weighting. The second group aims to identify Rossby wave trains as a whole, discounting individual troughs and ridges. The third group contains diagnostics which focus on physical mechanisms during the different phases of a Rossby wave train life cycle; they include the analysis of eddy kinetic energy and methods for quantifying Rossby wave breaking.

The different methods are analysed and systematically compared with each other in the framework of a two-month period in fall 2008. Each method more or less serves its designed purpose, but they all have their own strengths and weaknesses. Notable differences between the individual methods render an objective identification of a Rossby wave train somewhat elusive. Nevertheless, the combination of several techniques provides a rather comprehensive picture of the Rossby wave train life cycle, being broadly consistent with the expected behaviour from previous theoretical analysis.

## 1. Introduction

Mid-latitude atmospheric dynamics are characterised by synoptic-scale transient eddies, which manifest as a sequence of high and low pressure systems at the surface (Palmén and Newton, 1969). On the Northern Hemisphere these eddies are organised into so-called storm tracks (Hoskins and Valdes, 1990). As a consequence, statistical measures of transient eddy activity have a characteristic dependence on longitude. In the upper troposphere these transients appear in the form of Rossby wave trains (abbreviated as RWT henceforth), i.e. Rossby waves for which the amplitude envelope is modulated with longitude (Madden, 2007). The Rossby waves owe their existence to the

zonal waveguide which appears in the form of a sharp meridional gradient of potential vorticity (PV) (e.g. Schierz et al., 2004; Martius et al., 2010; Dritschel and McIntyre, 2008).

Recently, there has been increased interest in RWTs, because they may impact the prediction and predictability of mid-latitude weather systems (Shapiro, 2004). In particular, RWTs can prepare the ground for local severe weather. A representative example is the heavy precipitation event of August 2002, which led to catastrophic flooding in parts of Germany and the Czech Republic. This event was associated with a long-lived RWT, which originated off the coast of Japan and circumnavigated the major part of the Northern Hemisphere during the 10 d prior to the event (Grazzini and van der Grijn, 2003). Martius et al. (2008) showed that heavy precipitation events on the southern side of the Alps are, on average, associated with far-upstream precursory long-lived RWTs. The skillful prediction of RWTs is often a prerequisite for forecasting the synoptic-scale setting within which smaller-scale, high-impact weather systems evolve

\*Corresponding author

e-mail: ilona.glatt@uni-mainz.de

DOI: 10.1111/j.1600-0870.2011.00541.x

(Shapiro, 2004). Nonetheless, this potential has not been fully exploited yet. For instance, the heavy precipitation over Germany in August 2002 was poorly predicted, giving but scant indication for the actual event as little as three days ahead (Gibson, 2003). This motivates us to revisit the issue of Rossby wave trains.

Interestingly, the notion of a RWT and its life cycle eludes a strict definition despite its important role. Broadly speaking, a RWT is a perturbation of the atmospheric flow, close to a plane wave, for which the envelope is modulated on a spatial scale which is larger than the wavelength of the underlying carrier wave. The perturbation at some altitude can approximately be written as  $\Re A(\lambda, \phi, t) \exp(is\lambda)$ , where  $\Re$  denotes the real part,  $\lambda$  is longitude,  $\phi$  is latitude,  $t$  is time and  $s$  is the zonal wavenumber of the carrier wave. The smoothly varying envelope  $A$  has a local maximum and decays outside a specific region; its extent may well be planetary scale. The underlying carrier wave, in turn, ranges in the synoptic scale. RWTs have a finite life time on the order of several days. Conceptually, it is useful to distinguish three phases of a RWT life cycle: generation, propagation and decay.

There is quite an extensive literature about ‘wave packets’, a term which roughly refers to the same as ‘RWT’. Baroclinic wave packets have been detected both in models and observations (Lee and Held, 1993; Chang, 1993). Typical tracks of wave packet propagation were analysed by Chang and Yu (1999) and Chang (1999), and the characteristic spatial structure of baroclinic wave packets was investigated by Chang (2001). Different authors have used different methods to identify RWTs, suggesting that the results depend somewhat on the chosen method.

It would be interesting to know what aspects of a RWT are particularly prone to error and during which part of the life cycle errors are most likely to occur. This paper does a first step towards this goal. We shall explore to what extent the different aspects of a RWT can be diagnosed objectively using different methods. Arguably, one of the best methods to identify RWTs on weather maps is pattern recognition by the human brain. Of course this method is highly subjective, and different meteorologists would most likely come up with different identifications. Through systematic comparison we will identify the strengths and weaknesses of the methods, and learn which ones are useful to characterise the various stages of a RWT life cycle. In doing so, we restrict our attention to the zonal propagation by visualizing the flow on a given level in the form of a Hovmöller diagram (Hovmöller, 1949). By construction this type of diagram neglects certain aspects of the RWT evolution. For example, in the case of a split wave guide, as frequently occurring over Europe in springtime, the reduction of the data to one spatial dimension does not allow one to study each wave train in isolation. Figure 1 shows an example of a Hovmöller diagram, where RWTs have been identified subjectively. The red and green line in the figure illustrate how phase and group velocity can be obtained from this type of diagram.

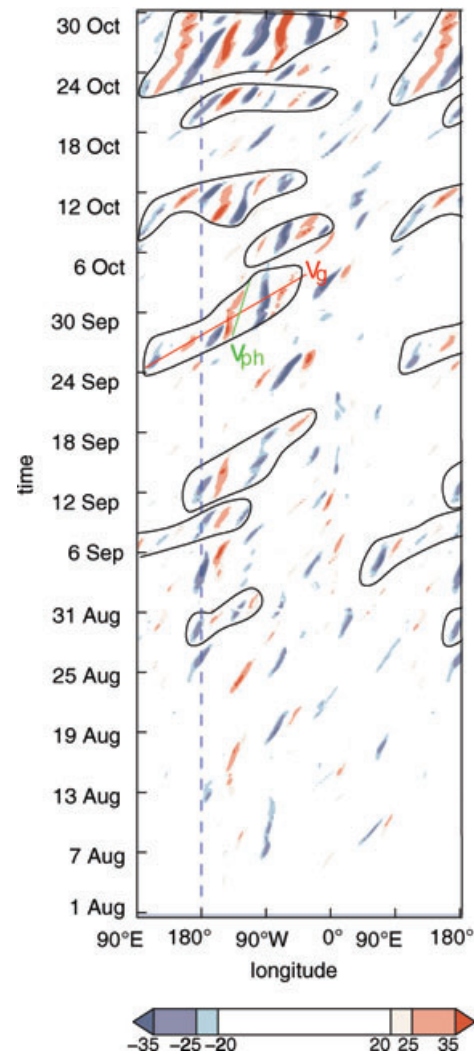


Fig. 1. Conventional Hovmöller diagram of the meridional wind  $v$  ( $\text{m s}^{-1}$ ; colour shaded) on the 330 K isentropic surface, averaged between  $40^\circ$  and  $60^\circ\text{N}$  for August through October 2008. For ease of viewing the region west of the date line was plotted twice in a wrap-around manner. Visually identified RWT are surrounded by a black line. The red and green line illustrate how the group and phase velocity can be obtained from this type of diagram.

Throughout this paper we shall confine our interest to the two-month period September through October 2008 in the Northern Hemisphere, which contains all stages of a RWT life cycle. This allows us not only to study the different methods in some detail, but also to relate them to the evolution on synoptic maps. Once the different diagnostics have been thoroughly understood, their future application in a more automated approach can provide statistical information from longer time periods. Eventually, this will yield climatological information about RWTs and their association with predictive skill.

The plan of our paper is as follows. In Section 2, we provide a brief synoptic overview of the chosen episode and show that it is

well suited for our purposes. Section 3 introduces the different diagnostic methods and provides a first comparison between them. Deeper insight is obtained in Section 4, where we place the outcome of each Hovmöller diagnostic in the context of the underlying synoptic maps. This reveals which aspects of the RWT evolution are captured in each diagnostic, and which ones are not. Finally, a summary and our conclusions will be given in Section 5.

## 2. Overview over the selected episode

For our analysis we chose the period of September and October 2008. Overall, this period was characterised by strong upper-level Rossby wave activity in the Northern Hemisphere, organised into distinct wave trains. According to our experience, the Rossby waves during this episode are somewhat larger in amplitude and more strongly non-linear than during a typical Northern Hemisphere winter month. The episode featured no less than ten tropical cyclones over the Atlantic basin, six of which underwent extratropical transition (ET) (Jones et al., 2003; Hoskins and Berrisford, 1988). The Rossby waves often evolved into a highly non-linear stage associated with streamers of potential vorticity (PV) and Rossby wave breaking, both of which are important mechanisms of the RWT decay (Nakamura and Plumb, 1994; Peters and Waugh, 1996, 2003; Postel and Hitchman, 1999; Martius et al., 2006b, 2007, 2008).

As an illustration of the weather systems during this period, we show in Fig. 2 a snapshot from September 5. On this day, Tropical Storm Josephine (marked Jos in Fig. 2) is located in the middle of the tropical Atlantic; at the same time Hurricane Ike (marked Ike in Fig. 2) is located northwest of Puerto Rico. The prominent low over Europe (marked L in Fig. 2) is the result of

a breaking Rossby wave over the North Atlantic on August 30 and 31. It caused severe weather like strong winds and intense rainfall WMO Bulletin (2008). The western high PV-anomaly (marked Cut in Fig. 2) results from a cut-off low that reconnected to the stratospheric PV-reservoir.

In summary, the chosen episode contains a wealth of different phenomena associated with RWTs and appears, therefore, suitable for our purpose.

## 3. Rossby wave train diagnostics

This chapter introduces the diagnostic methods to be discussed in this paper. These diagnostics differ not only in their methodology and focus of analysis, but also in the preprocessing of the data. In this regard, we follow as closely as possible the description published in the original papers.

Unless indicated otherwise, our meteorological data are the operational analyses of the European Centre for Medium Range Weather Forecasts (ECMWF) with a spatial resolution of  $0.5^\circ$  in both longitude and latitude, and with a temporal resolution of 6 h.

### 3.1. Weighting function Hovmöller diagram

A conventional Hovmöller diagram of the upper tropospheric meridional wind was already shown earlier in Fig. 1. The plotted quantity is averaged over a latitudinal band whose boundaries have to be specified in advance. This renders the automatic application to long time series somewhat difficult, because the overall eddy activity may shift in latitude with time (e.g. as a function of season). To avoid this difficulty, we designed a novel

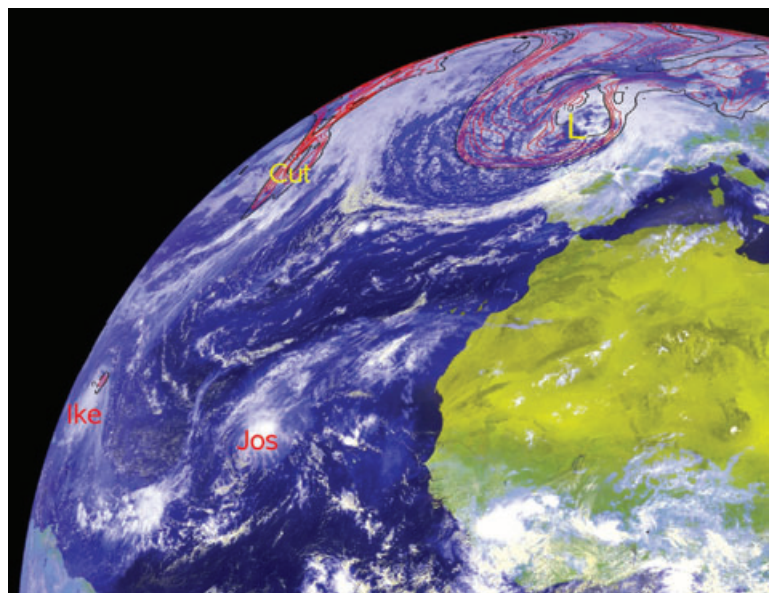


Fig. 2. False colour composite Meteosat-9 SEVIRI image for 5 September 2008, 12:00 UTC. Superimposed are contours of potential vorticity (PV) on the 330 K-isentrope (black: 2 PVU-contour, red: 4, 6, 8, 10 PVU-contours, with 1 PVU =  $10^{-6} \text{ K m}^2 \text{ kg}^{-1} \text{ s}^{-1}$ ).

method following an idea of Ambaum (2008). First, a flow-dependent latitudinal weighting function is defined through

$$w(\phi) = N \int_0^{2\pi} (v - [v])^2 \cos \phi \, d\lambda, \quad (1)$$

where  $\phi$  denotes latitude,  $\lambda$  denotes longitude,  $v = v(\lambda, \phi)$  is the meridional wind on the level of interest and the angle brackets  $[\dots]$  denote a zonal average. The weighting function  $w(\phi)$  aims to capture the zonal mean position of the waveguide by favouring those latitudes where the longitudinal variance of  $v$  is large. The normalization constant  $N$  is chosen such that  $\int_0^\pi w(\phi) \, d\phi = 1$ . In order to avoid very long tails,  $w(\phi)$  is set to zero where the original value is below 0.01; afterwards, it is normalized again as described above. The weighting function is computed anew at every time step, that is, every 6 h.

For illustration, we consider the meridional wind  $v$  on the isentropic surface  $\theta = 330\text{K}$ . The variable to be plotted in this so-called weighting function Hovmöller diagram is computed through convolution with  $w(\phi)$ , that is,

$$\hat{v}(\lambda) = \int_0^\pi w(\phi) v(\lambda, \phi) \, d\phi. \quad (2)$$

Figure 3 shows the result for the period under consideration. In addition to the individual maxima and minima of the  $\hat{v}$ -field, the

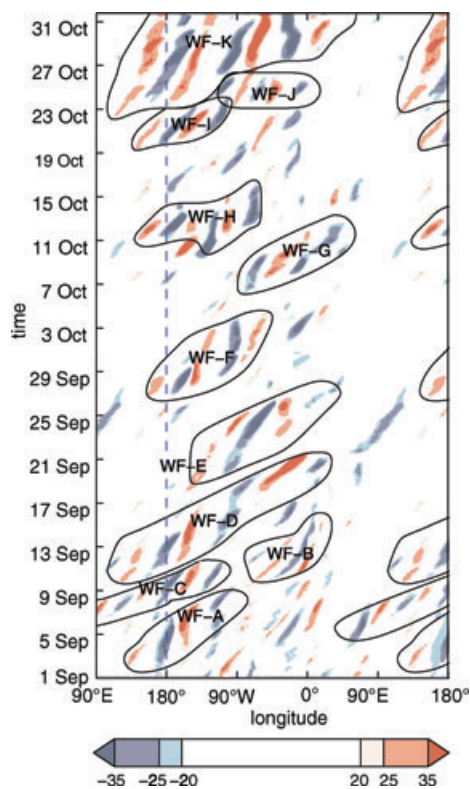


Fig. 3. Weighting function Hovmöller diagram of the meridional wind  $\hat{v}$  ( $\text{ms}^{-1}$ , colour shaded) at  $\Theta = 330\text{K}$  for September and October 2008. Visually identified RWT are surrounded by a black line and labelled WF-A to WF-K.

figure identifies the different RWTs through surrounding solid lines (labelled with letters WF-A to WF-K). Consistent with our definition in the introduction<sup>1</sup>, these RWTs were subjectively identified as coherent series of at least three consecutive extrema of  $\hat{v}$ . Quantities like phase and group velocities associated with the Rossby waves can be diagnosed visually (Hovmöller, 1949).

This diagram resembles the conventional Hovmöller diagram from Fig. 1. However, there are differences in the details. For instance, the occurrence of negative  $\hat{v}$  around  $90^\circ\text{E}$  from September 22 through 28 in Fig. 3 is almost completely absent in Fig. 1. We shall come back to this discrepancy in Section 4.2.

### 3.2. Waveguide Hovmöller diagram

The method introduced in the previous section approximately accounts for changes in the zonal mean position of the extratropical waveguide. However, this may not be sufficient because each Rossby wave may perform significant latitudinal excursions on its way around the earth. As a consequence, the RWT may locally leave the latitudes with significant weight and, therefore, spuriously disappear from the Hovmöller diagram. An approach which avoids this effect is the so-called refined Hovmöller diagram of Martius et al. (2006a), here called ‘waveguide Hovmöller diagram’. Broadly speaking, it is obtained by averaging the considered meteorological variable along the Rossby waveguide.

The method is based on the fundamental physical mechanism of conservative Rossby wave dynamics (Rossby, 1945). Meteorological quantities of interest are investigated on an upper tropospheric isentropic surface which transects the tropopause. The location of the waveguide is identified through a specific value of Ertel PV (Ertel, 1942) corresponding to the dynamical tropopause on this isentrope, for example, the 2 PVU contour line. Depending on the choice of the isentropic surface, the emphasis is either on the extratropical or the subtropical waveguide. The respective meteorological variable is averaged over a  $10^\circ$  latitudinal band that is centred on the selected PV contour line. In the case of an overturning PV-contour, the method involves an average over several parts of the tropopause for a given longitude.

Figure 4(a) shows the waveguide Hovmöller diagram for the meridional wind  $v$  on  $\theta = 330\text{K}$ . Phase and group velocity associated with the Rossby waves can be diagnosed as before. Again, wave trains have been identified subjectively as a series of at least three consecutive extrema of  $v$ ; they are labelled with letters from WG-A to WG-J. Comparison with the two previous Hovmöller diagrams shows an overall agreement regarding the number and appearance of RWTs, but there are differences in the details. For instance, the wave train crossing the date line around September 13 appears somewhat more coherent in the waveguide

<sup>1</sup> ... requiring the wave envelope to be of larger longitudinal extent than the wavelength of the underlying carrier wave.

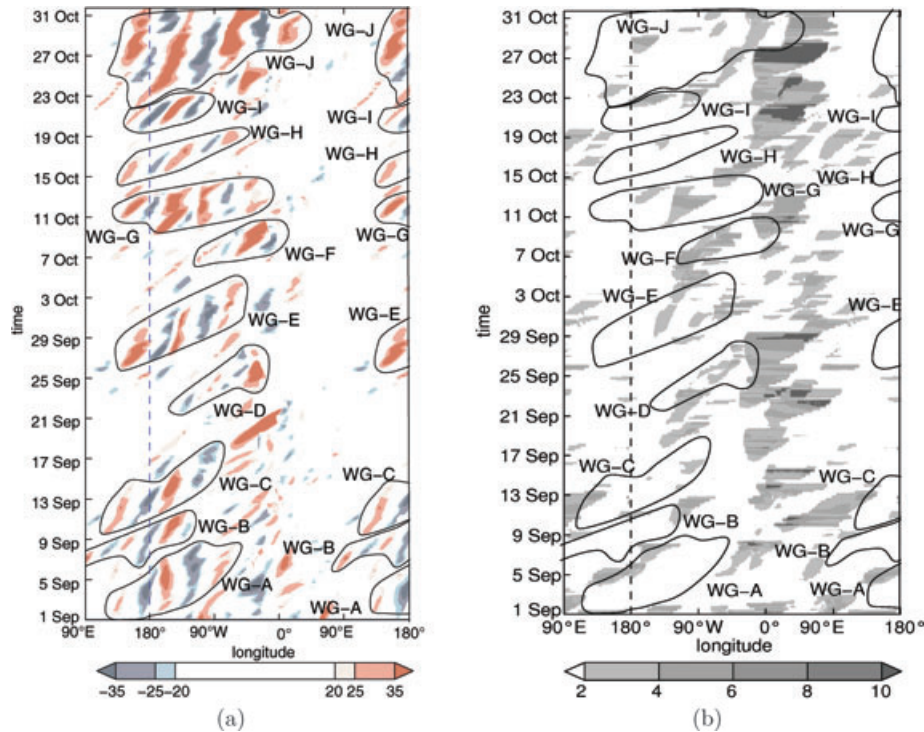


Fig. 4. (a) Waveguide Hovmöller diagram of the meridional wind  $v$  ( $\text{ms}^{-1}$ , colour shaded) at  $\Theta = 330$  K for September and October 2008. Identified RWTs are circled and marked by WG-A to WG-J. (b) Length of the 2 PVU contour line at  $\Theta = 330$  K for September and October 2008. (The contour length is normalized as described in Martius et al. (2006a); colour shaded). The position of the RWTs identified in (a) is also shown in (b).

Hovmöller diagram than in the other two types of Hovmöller diagrams. On the other hand, the weighting function Hovmöller diagram in Fig. 3 features a strong and well-defined wave train over North America and the Atlantic between September 20 and 26 (WF-E), which is much less distinct in the waveguide Hovmöller diagram (WG-D).

The method of Martius et al. (2006a) also provides the length of the chosen PV contour for a given longitude segment. According to the authors, this can be taken as an indicator for Rossby wave breaking. The argument essentially follows McIntyre and Palmer (1985), who defined wave breaking as an irreversible mixing of the potential vorticity. The Hovmöller diagram for the contour length diagnostic is shown in Fig. 4(b). Although the details of this diagram appear rather complicated, there is a predominant occurrence of enhanced contour length close to and somewhat eastward of the Greenwich meridian. This is consistent with the known fact that the wave trains associated with the North Atlantic storm track typically reach their mature stage in this region (cf. Fig. 1), leading to Rossby wave breaking and the formation of PV streamers over the North Atlantic and Europe.

### 3.3. Eddy kinetic energy

In the past, eddy kinetic energy has played an important role in understanding the development associated with upper tropospheric Rossby waves, especially in connection with the storm-

tracks (Chang, 1999; Orlandi and Katzfey, 1991; Chang and Orlandi, 1993; Orlandi and Sheldon, 1995) and in quantifying the impact of ET on midlatitude development downstream (Harr and Dea, 2009). The budget of eddy kinetic energy was shown to be well suited to diagnose the physical processes by which individual troughs and ridges build and decay, and how the wave energy is transferred between them.

Here, we follow the development of Orlandi and Katzfey (1991), and Orlandi and Sheldon (1995). They distinguish between the basic state and the disturbance. The basic state is defined as a running mean with a window width of 30 d centred around the day of interest. For the horizontal wind  $\mathbf{v}$ , this yields  $\mathbf{v} = \mathbf{v}_m + \mathbf{v}'$  where subscript  $m$  denotes the basic state and the prime denotes the deviation therefrom (with analogous notation for other variables). Specific eddy kinetic energy is defined as

$$K_e = \frac{1}{2}(\mathbf{v}')^2. \quad (3)$$

Since, we are mostly interested in the horizontal propagation of RWTs, we follow Harr and Dea (2009) restricting our attention to the vertically integrated budgets (on pressure levels from 1000 to 100 hPa, henceforth denoted by the overbar symbol) of eddy kinetic energy, that is, we consider  $\overline{K_e}$  instead of  $K_e$ .

Figure 5 displays the evolution of  $\overline{K_e}$  in a conventional Hovmöller diagram (averaged between  $40^\circ$  and  $60^\circ$  latitude north). As in the previous Hovmöller plots, eddy kinetic

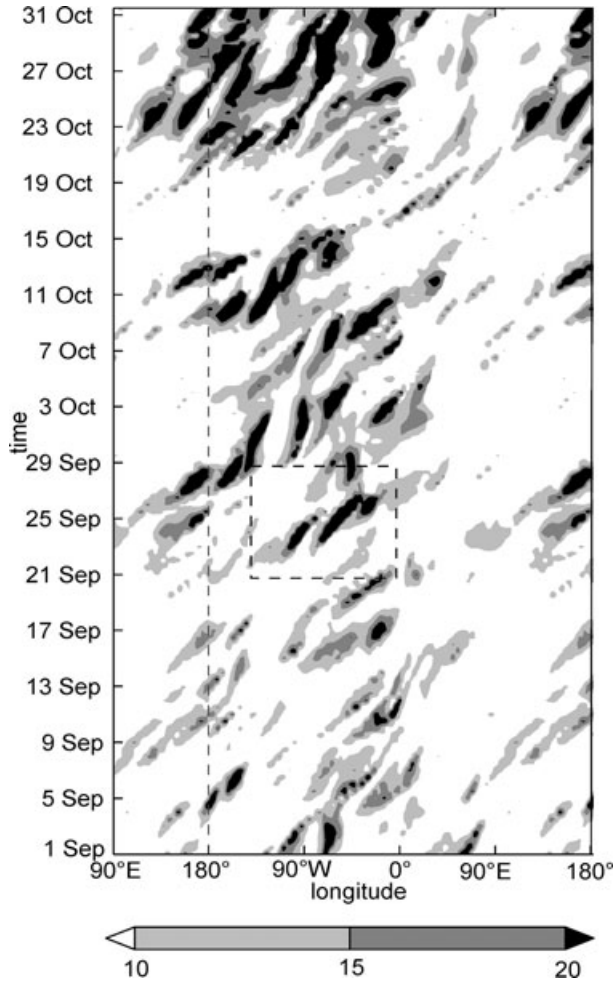


Fig. 5. Hovmöller diagram of  $\overline{K_e}$  (in  $10^5 \text{Jm}^{-2}$ ) for the episode September and October 2008. The data are vertically integrated between 1000 and 100 hPa and averaged over a latitude belt between  $40^\circ$  and  $60^\circ\text{N}$ . The temporal resolution of the data for this analysis is 12 h. The dashed box refers to the area of Fig. 8.

energy indicates generally reduced Rossby wave activity around western Eurasia. However, in contrast to the previous diagnostics, it is less straightforward to identify RWTs from this diagram. Therefore, we refrain from labelling individual RWTs.

In order to derive a budget equation for  $\overline{K_e}$ , we combine eqs (2.3) and (2.4) from Orlandi and Sheldon (1995). Assuming that the vertical wind is small at the upper and lower limit of our integration, the vertical flux divergences vanish upon integration and we are left with the following equation

$$\frac{\partial \overline{K_e}}{\partial t} = \underbrace{\overline{-\omega\alpha}}_A - \underbrace{\overline{\mathbf{v}' \cdot (\mathbf{v}' \cdot \nabla_p \mathbf{v}_m)}}_B - \underbrace{\overline{\nabla_p \cdot (\mathbf{v}'\phi')_{(a)}}}_C - \underbrace{\overline{\nabla_p \cdot (\mathbf{v}K_e)}}_D + \text{Residue} \quad (4)$$

The subscript  $p$  indicates that the derivatives are calculated on pressure levels. The term A denotes the baroclinic conversion of eddy potential energy to eddy kinetic energy; term B denotes the barotropic conversion of kinetic energy between the eddies and the mean flow; the term C (with subscript  $a$ ) is the so-called ageostrophic geopotential flux, defined in (2.5) in Orlandi and Sheldon (1995); the term D is the divergence of horizontal eddy kinetic energy flux. The residue contains all other terms including eddy dissipation; the above cited papers have shown that the residue is small in synoptic-scale applications which we consider here.

As shown in Orlandi and Sheldon (1995), the term C typically describes downstream radiation of  $\overline{K_e}$ . Term D, on the other hand, reflects the advection of existing features of  $\overline{K_e}$  by the total wind; this can be seen by noting that  $\mathbf{v} \approx \mathbf{v}_g$  (with  $\mathbf{v}_g$  denoting the geostrophic wind) and, hence,  $\overline{\nabla_p \cdot (\mathbf{v}K_e)} \approx \overline{\mathbf{v}_g \cdot \nabla_p \overline{K_e}}$ . Since both C and D are divergences of a flux, they vanish upon integration over the entire domain (assuming the flux to vanish at the northern and southern boundary). Hence, C and D can only redistribute eddy kinetic energy without net generation or destruction. On the other hand, terms A and B are generally non-zero even upon global integration; they describe generation of total eddy kinetic energy through transfer from other forms of energy such as eddy available potential energy (term A) and kinetic energy of the mean flow (term B).

We first consider terms A and B shown in Fig. 6. Evidently, the baroclinic generation term A is mostly positive with largest values around the date line and at about  $70^\circ\text{W}$ . This is consistent with the idea of baroclinic downstream development close to the entrance region of a storm track (Chang and Orlandi, 1993). The barotropic conversion term B, on the other hand, tends to be predominantly negative, with largest negative values close to the Greenwich meridian and at about  $150^\circ\text{W}$ . Also note that the typical amplitude of term A is somewhat larger than the typical amplitude of term B. The overall behaviour is consistent with the accepted picture for the evolution of baroclinic eddies within a storm track (Lee and Held, 1993): there is baroclinic generation of eddy kinetic energy at the entrance of the storm track (e.g. close to the date line in our case), while further downstream there is loss of eddy kinetic energy mostly through barotropic conversion (e.g. at the end of the Atlantic storm track around the Greenwich meridian in our case).

The terms C and D are plotted in Fig. 7. Both figures are characterized by adjacent areas of large positive and negative values, indicating redistribution of  $\overline{K_e}$  over short horizontal distances. As explained before, the patterns associated with term D simply describe advection of eddy kinetic energy by the total wind. On the other hand, term C can be interpreted as the eastward radiation of eddy kinetic energy in connection with ‘downstream development’ (Orlandi and Sheldon, 1995). In the past term C has been used to identify Rossby wave trains (Chang, 2000). This motivated us to subjectively identify wave packets in Fig. 7 (a) and to label them with letters AG-A to AG-L.

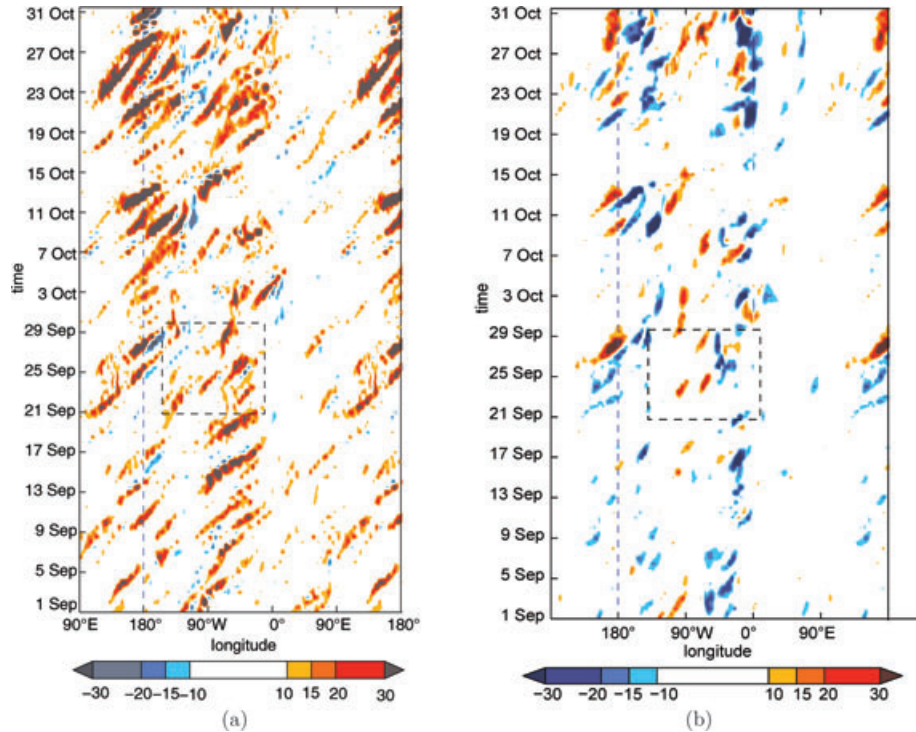


Fig. 6. Hovmöller diagrams for September and October 2008 of the generation of the eddy kinetic energy. (a) Term A ( $\text{Wm}^{-2}$ ) and (b) term B ( $\text{Wm}^{-2}$ ). All quantities are vertically integrated between 1000 to 100 hPa and averaged over a latitude belt between  $40^\circ$  and  $60^\circ$  N. The temporal resolution of the data for this analysis is 12 h. The dashed box refers to the area of Fig. 8.

The eastward radiation of eddy kinetic energy is further illuminated in Fig. 8, which focuses on a specific episode that is indicated through the dashed boxes in Figs 5 and 7(a). Eddy kinetic energy flows from an existing upstream eddy (marked by  $\bar{K}_e$ -maxima in Fig. 8) situated around  $100^\circ\text{W}$  into an amplifying downstream eddy located around  $80^\circ\text{W}$ . This energy transfer materializes in the form of a dipole structure with positive values (divergence) in the eastern part of the degenerating eddy and negative values (convergence) in the eastern part of the developing eddy. While the above mechanism describes the  $\bar{K}_e$ -transfer between two distinct eddies, the evolution of the downstream eddy is also influenced by simple advection of eddy kinetic energy (term  $D$ ). Furthermore, Fig. 6 reveals that the amplification of the downstream eddy is also supported by baroclinic and barotropic  $\bar{K}_e$ -production. In this particular case, both  $A$  and  $B$  contribute to eddy growth. This is consistent with the finding of Chang (2000), who showed that different mechanisms, like downstream development and barotropic and baroclinic growth, are involved in the evolution of the eddy kinetic energy budget of the troughs and ridges in a wave packet.

### 3.4. Rossby wave train objects

We have developed a novel method to objectively identify and characterize RWTs. It primarily aims to diagnose Rossby wave trains as a whole, discounting the phase information contained

in the sequences of positive and negative values of the meridional wind. The method is designed to objectively determine RWT properties such as their amplitude, time and location of occurrence, and their group velocity.

Point of departure is the meridional wind  $v(\lambda, \phi)$  on an upper tropospheric isentrope. For each latitude we compute the wave envelope  $A(\lambda, \phi)$  with the help of a Hilbert transform (Zimin et al., 2003). Simultaneously, we apply a filter for zonal wavenumbers in Fourier space. In this paper, we restrict our attention to zonal wavenumbers  $s = 4-15$ . Finally, for presentation in the form of a Hovmöller diagram, the envelope is convoluted with  $w(\phi)$  from (1) to obtain  $\hat{A}(\lambda)$ .

Based on this Hovmöller diagram, we proceed to define RWT objects. Following Davis et al. (2006), we first smooth the data from the envelope Hovmöller diagram by applying a running mean in both longitude (over  $1.5^\circ$ ) and time (18 h). Afterwards, a velocity threshold (here:  $20 \text{ m s}^{-1}$ ) is chosen, and the envelope is set to zero in regions where the amplitude is below the threshold. This eliminates regions with weak or no Rossby wave activity from further consideration. The non-zero parts of the truncated envelope are reset to their original (i.e. unsmoothed) values. Each connected region with a non-zero envelope is identified as an object representing a RWT.

Note that an increase of the velocity threshold may break a single object into two or more smaller objects, and vice versa (cf. the ‘camel effect’ in Wernli et al., 2008). In order to reduce this

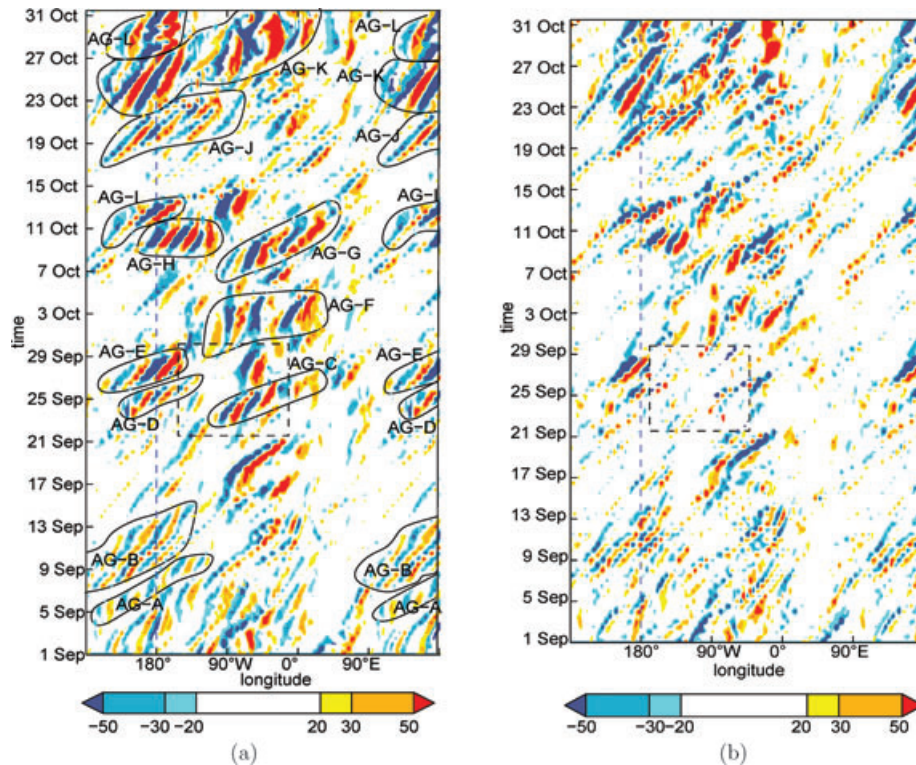


Fig. 7. Hovmöller diagram for September and October 2008 of the convergence of eddy kinetic energy. (a) Term C (divergence of the ageostrophic geopotential flux) ( $\text{Wm}^{-2}$ ) and (b) term D ( $\text{Wm}^{-2}$ ). All quantities are vertically integrated between 1000 to 100 hPa and averaged over a latitude belt between  $40^\circ$  and  $60^\circ$  N. The temporal resolution of the data for this analysis is 12 h. The dashed box refers to the area of Fig. 8.

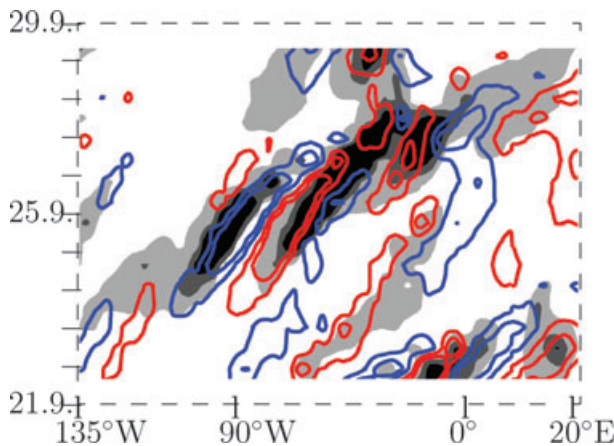


Fig. 8. Magnified combination of the dashed boxes in Figs 5 and 7(a). Shaded: eddy kinetic energy [ $(10, 15, 20) \times 10^5 \text{ Jm}^{-2}$ ]; contours: term C, blue:  $(20, 50) \cdot (\text{Wm}^{-2})$ ; red:  $(-20, -50) \cdot (\text{Wm}^{-2})$ .

sensitivity, we merge distinct RWT objects into a single one if the following conditions are met. First, objects are only merged if the distance between their centres of mass is less than  $10^\circ$  and 12 h, respectively. In addition, the later object has to be located in the direction of the group velocity of the earlier object. The

group velocity is obtained from the slope of the principal axis of inertia of the respective object. Finally, very small objects are eliminated by requiring a minimum number of gridpoints (600 in our case) for each object.

The objects which we obtained for our episode are denoted by O-A to O-P. They are displayed in Fig. 9, together with their principal axis of inertia indicating the corresponding group velocity. Due to their compact appearance, the RWTs are easy to identify. Most of the objects depicted in Fig. 9 can be assigned to a corresponding RWT in Fig. 3 and vice versa. For example, the objects O-H, O-I, O-K and O-L appearing in Fig. 9 can be recognized as coherent RWTs WF-E to WF-H in Fig. 3. Nevertheless many objects, especially in the first half of September, do not correspond to a RWT in any other diagram.

Clearly, our algorithm depends on the choice of the velocity threshold, and both the number of objects and their properties may change as the threshold is varied. Applying our method thus requires this threshold to be chosen carefully. For instance, the optimum value may depend on the considered surface or the season. Nevertheless, our method is objective in the sense that once a threshold has been chosen large data sets can automatically be screened using the same criteria throughout. As stated above, the latter is considered a key advantage of this method.

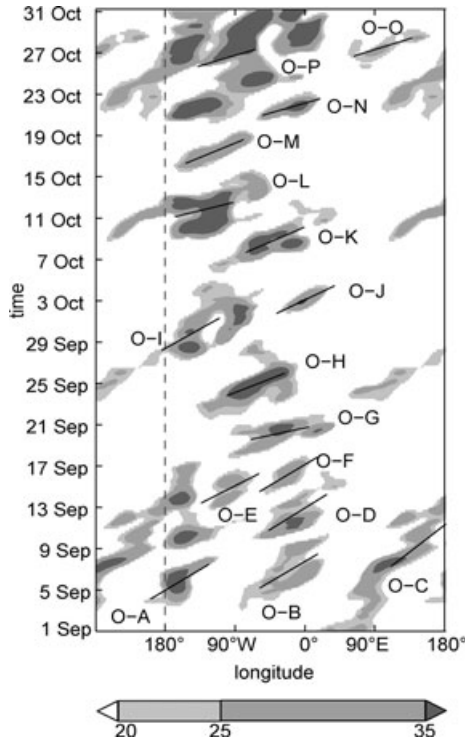


Fig. 9. Identified objects ( $\text{ms}^{-1}$ , shaded contours) at  $\Theta = 330 \text{ K}$ ; the lowest contour level is identical to object identification threshold. Black solid lines indicate the principal inertia axis, whose gradient gives the group velocity.

### 3.5. Plumb flux

Another method for diagnosing wave generation, propagation and decay is based on conservation laws for the wave activity and the corresponding flux (Scinocca and Shepherd, 1992). This idea was pioneered by Eliassen and Palm (1961), who recognized that wave energy in shear flow can grow or decay without any non-conservative processes, preventing a straightforward interpretation of RWT propagation. The so-called Eliassen-Palm flux, on the other hand, does not suffer from this problem. It is a zonally averaged quantity and allows one to diagnose wave propagation in the latitude–altitude plane (Andrews and McIntyre, 1976). Plumb (1985) generalized this concept to three dimensions, thus including the possibility of diagnosing transport in the longitudinal direction. Like our RWT objects, the Plumb flux discounts any phase information and focuses on the RWT as a whole. Plumb’s formulation applies to small-amplitude stationary waves on a zonally symmetric basic state. In the WKB-limit, the Plumb flux is proportional to the group velocity of the Rossby wave.

An extended version of this concept was introduced by Takaya and Nakamura (2001), who derived a wave activity flux applicable to either stationary or migratory quasigeostrophic eddies on a zonally varying basic flow. It requires the phase velocity of the

eddies to be determined. We suspect that the differences between the two formulations are small, because the zonal phase velocity of our Rossby waves is very small and they can, thus, be considered as quasi-stationary. By design, the Takaya-Nakamura flux approaches the Plumb flux for stationary waves on a zonally symmetric basic state. For simplicity we therefore restrict our attention to the Plumb flux.

Despite theoretical limitations, the Plumb flux has been applied to real flows (Nishii and Nakamura, 2004; Peters et al., 2007). It captured quite well the propagation of the Rossby waves in the upper troposphere and can be used to identify wave trains. We use the formulation which implicitly contains the geostrophic and thermal wind relations (Eq. (7.1) in plumb, 1985). Here, perturbations are defined as deviations from the zonal mean. Since we are mainly interested in horizontal wave propagation, we restrict our attention to the horizontal components of the flux. On the sphere, they are given by

$$\begin{pmatrix} F_\lambda \\ F_\phi \end{pmatrix} = \frac{p}{p_0} \cos \phi \begin{pmatrix} v'^2 - \frac{1}{2\Omega a \sin 2\phi} \frac{\partial(v'\Phi')}{\partial \lambda} \\ -u'v' + \frac{1}{2\Omega a \sin 2\phi} \frac{\partial(u'\Phi')}{\partial \lambda} \end{pmatrix}, \quad (5)$$

where  $p$  is the pressure,  $p_0 = 1000 \text{ hPa}$ ,  $(u', v')$  are the horizontal geostrophic wind perturbations,  $\Phi'$  is the perturbation geopotential,  $\Omega$  is the angular velocity of the Earth’s rotation and  $a$  denotes the radius of the Earth. Before evaluating the right hand side of (5), the fields are smoothed with a running mean over 3 d and  $4^\circ$  in longitude. The resulting flux components are averaged meridionally between  $40^\circ$  and  $60^\circ \text{ N}$  and vertically between 400 and 100 hPa. We thus arrive at an averaged version  $(\bar{F}_\lambda, \bar{F}_\phi)$  of the Plumb flux, characterizing horizontal propagation of wave activity in the mid-latitude upper troposphere.

Hovmöller diagrams of the components  $\bar{F}_\lambda$  and  $\bar{F}_\phi$  are shown in Fig. 10. Areas of strong fluxes  $\bar{F}_\lambda$  were identified and subjectively grouped. According to the design of Plumb’s method, these groups should broadly correspond to RWTs. Using this method we identified eight RWTs labelled by P-A to P-H in the figure. They mainly occur between  $120^\circ \text{ E}$  and  $0^\circ$ , whereas the fluxes nearly vanish over Europe. The predominance of positive  $\bar{F}_\lambda$ -values (negative values are about one order of magnitude less and are not shown) is consistent with eastward propagation of the Rossby wave packets associated with the RWTs. The patterns of  $\bar{F}_\phi$  point to the redistribution of wave activity in the meridional direction [see Fig. 10(b)]. There is a general predominance of equatorward flux (negative values of  $\bar{F}_\phi$ ) corresponding to poleward transport of angular momentum, particularly during the mature and final stages of a wave train life cycle (see Fig. 10(b) for P-C, P-D and P-G). This is consistent with the general picture of an eddy driven jet, where barotropic eddy motions feed momentum back into the jet (Lee, 1997). It is also consistent with our earlier analysis of eddy kinetic energy which indicated a predominance of a barotropic energy sink towards the end of our Rossby wave trains.

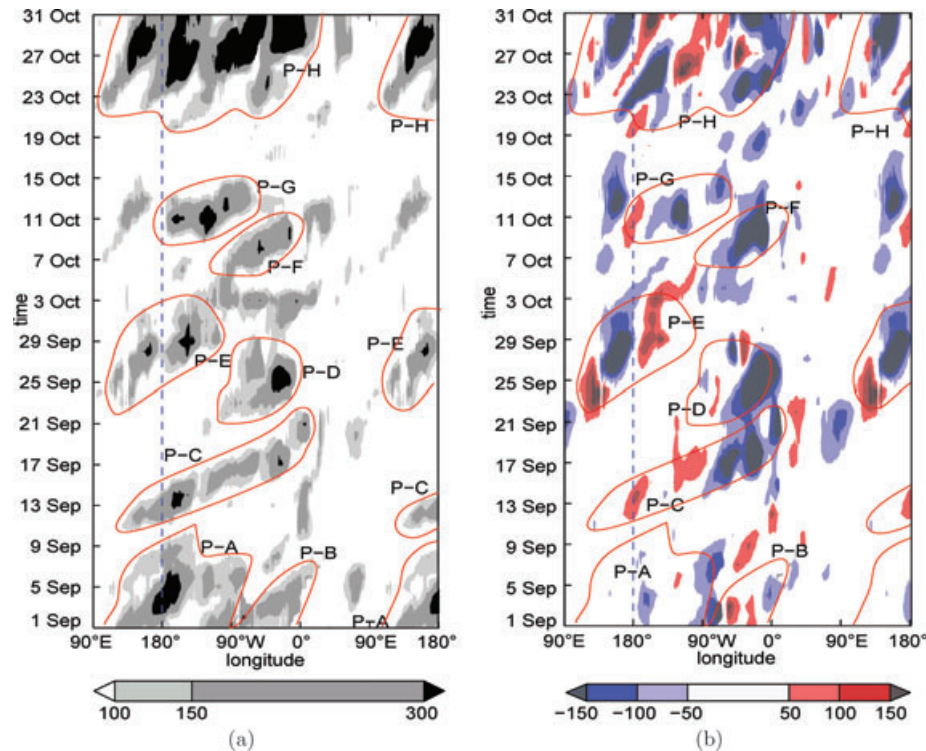


Fig. 10. Hovmöller diagrams of the horizontal components of the Plumb-flux vector  $\bar{F}_\lambda$  and  $\bar{F}_\phi$  for September and October 2008. (a)  $\bar{F}_\lambda$  ( $\text{m}^2 \text{s}^{-2}$ , shaded), positive values indicate flux to the east. (b)  $\bar{F}_\phi$  ( $\text{m}^2 \text{s}^{-2}$ , colour shaded) positive values indicate flux to the north. RWTs were subjectively identified in panel (a) and are depicted in both panels using red lines.

### 3.6. Rossby wave breaking

As mentioned earlier, the final stage of a RWT life cycle is often associated with Rossby wave breaking. Thus, it is of interest to diagnose wave breaking in some detail. Here, we consider the method of Gabriel and Peters (2008), who classify the breaking events into four types: cyclonic poleward (P1), cyclonic equatorward (LC2), anticyclonic poleward (P2) and anticyclonic equatorward (LC1). Climatologically, each type is associated to a preferred geographical region.

Here, we only provide a short summary of the method, for the details the reader is referred to Gabriel and Peters (2008). First, the meteorological fields are preprocessed using various averages to remove small-scale contributions. Then, Rossby wave breaking is identified through reversed meridional gradients of Ertel PV on an isentropic surface (i.e.  $\partial \text{PV} / \partial \phi < 0$ ); this essentially follows the suggestion of McIntyre and Palmer (1983), who considered planetary wave breaking in the stratosphere. Note, that the overturning itself is not necessarily irreversible. (Although in most cases is eventually leads to irreversible mixing and, thus, wave breaking in the strict sense.) Thus the wave train can actually persist for some time after this type of ‘breaking’ has been diagnosed. Within the region of wave breaking, cyclonic and anticyclonic breaking is distinguished using the sign of the meridional component of the Plumb Flux,  $F_\phi$ , with

$F_\phi > 0$  corresponding to cyclonic and  $F_\phi < 0$  corresponding to anticyclonic wave breaking (cf. Esler and Haynes, 1999). In addition, poleward and equatorward breaking is distinguished on the basis of the diffuence and/or confluence of the geostrophic wind; the algorithm discards 10% of all events, namely those which are neither clearly poleward nor clearly equatorward. The intensity of the breaking is quantified by an index, which is defined at each grid point as the value of  $F_\phi$ . Note that this index does not contain any measure for the strength of PV overturning. As a consequence, it may show discontinuous behaviour in time. For instance, in the presence of large values of  $F_\phi$  the onset of PV overturning is accompanied by the index jumping from zero to a large value. Also, the index may be zero despite strong wave breaking if  $F_\phi$  happens to be zero. We, therefore, consider this index to primarily quantify the meridional transport of zonal momentum during the mature phase of a Rossby wave. Hovmöller diagrams for this index (Fig. 11) reveal a dominance of LC1 and P2 events. As expected, the P2 and LC1 events occur mainly at the end of the RWTs over the eastern North Atlantic. This finding is consistent with the results of the previous sections indicating that most RWTs develop into a non-linear stage before reaching Europe. Furthermore, the dominance of anticyclonic wave breaking in this longitude range corresponds to large negative values of  $\bar{F}_\phi$  [see Fig. 10(b)]. Interestingly, LC1 events with high values in the wave breaking index occur

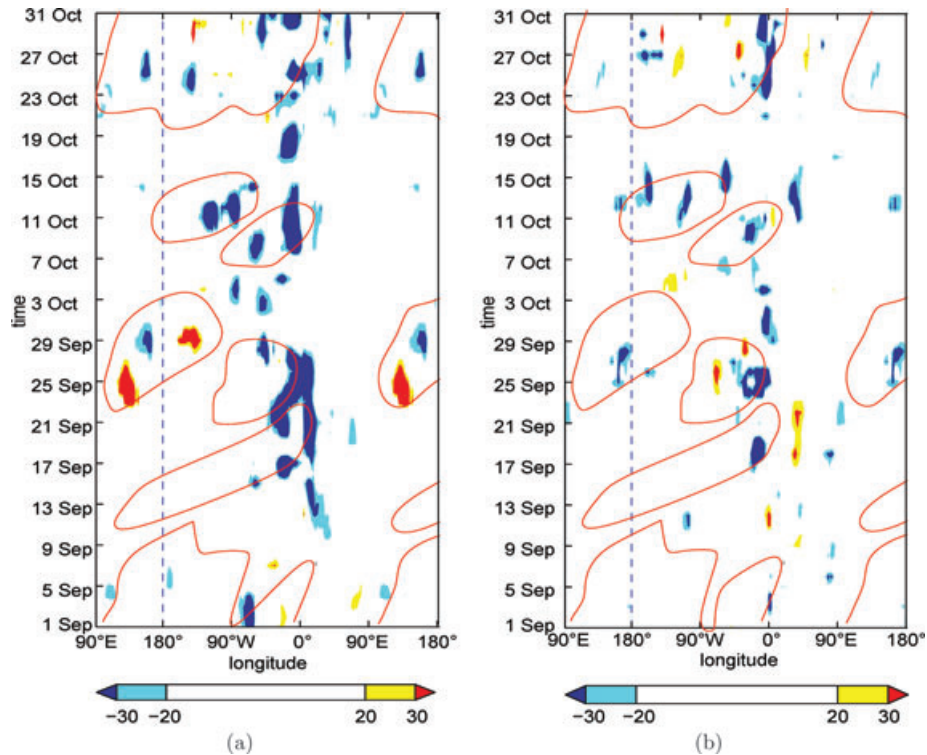


Fig. 11. Hovmöller diagrams of the wave breaking index for September and October 2008. (a) P1 ( $\text{m}^2 \text{s}^{-2}$ , positive values) and P2 ( $\text{m}^2 \text{s}^{-2}$ , negative values). (b) LC1 ( $\text{m}^2 \text{s}^{-2}$ , negative values) and LC2 ( $\text{m}^2 \text{s}^{-2}$ , positive values).

over all longitudes, although they slightly cluster around  $10^\circ\text{W}$ . Cyclonic breaking events (P1 and LC2) occur less frequently and yield lower index values. There are only two P1-events with higher index values which occur during the life time of the RWT P-E. Other cyclonic breaking events occur more erratically.

For some breaking events two different types (e.g. LC1 and P2 for P-C, P-G and P-H) classify the same breaking event. This occurrence of two different wave breaking types in the Hovmöller diagram at the same time and location is possible, because a Hovmöller diagram involves a latitudinal average, while wave breaking may occur at any latitude.

It is interesting to compare this four-type classification of Rossby wave breaking with the contour length diagnostic from Section 3.2. A comparison of Figs. 4(b) and 11 shows that some features are similar for both diagnostics. In particular, both indicate enhanced wave breaking towards the end of the Atlantic storm track. However, there are also substantial differences, and we shall come back to this issue in the following section.

#### 4. Comparison and Discussion

We shall now systematically compare the different diagnostics with each other, aiming to understand the differences and their strengths and weaknesses. This will be achieved through reference to the underlying synoptic situation.

##### 4.1. A large-amplitude Rossby wave train

In this section, we focus on the 8-day episode from October 24–31. It was characterized by a large-amplitude RWT, which moved from eastern Asia to Europe. It reached its non-linear stage over the eastern Atlantic around October 28. During the whole period highly non-linear wave breaking took place around  $45^\circ\text{E}$ . Figure 12 shows a sequence of daily maps characterizing the synoptic situation in the upper troposphere.

The first three Hovmöller diagrams in Fig. 13 include full phase information of the underlying Rossby wave. Following the original paper by Hovmöller, we call them ‘trough-and-ridge Hovmöller diagrams’<sup>2</sup>. The different extrema in these diagrams are labelled with capital letters consistent with Fig. 12. Essentially, all large-scale troughs and ridges from Fig. 12 are represented by this group of Hovmöller diagrams. Generally, the extrema in  $v$  have a larger amplitude in the waveguide Hovmöller diagram (panel c) compared to the other two (panel a and b). This is particularly true for the features labelled E and G. Variation of

<sup>2</sup> Note that we consider the meridional wind, so strictly speaking the extrema in our Hovmöller diagrams represent the sides of the troughs and ridges, rather than the troughs and ridges themselves. On the other hand, Hovmöller (1949) used the geopotential height, thus his extrema do, indeed, represent troughs and ridges. Nevertheless, for ease of terminology we stick to the term ‘trough-and-ridge Hovmöller diagram’.

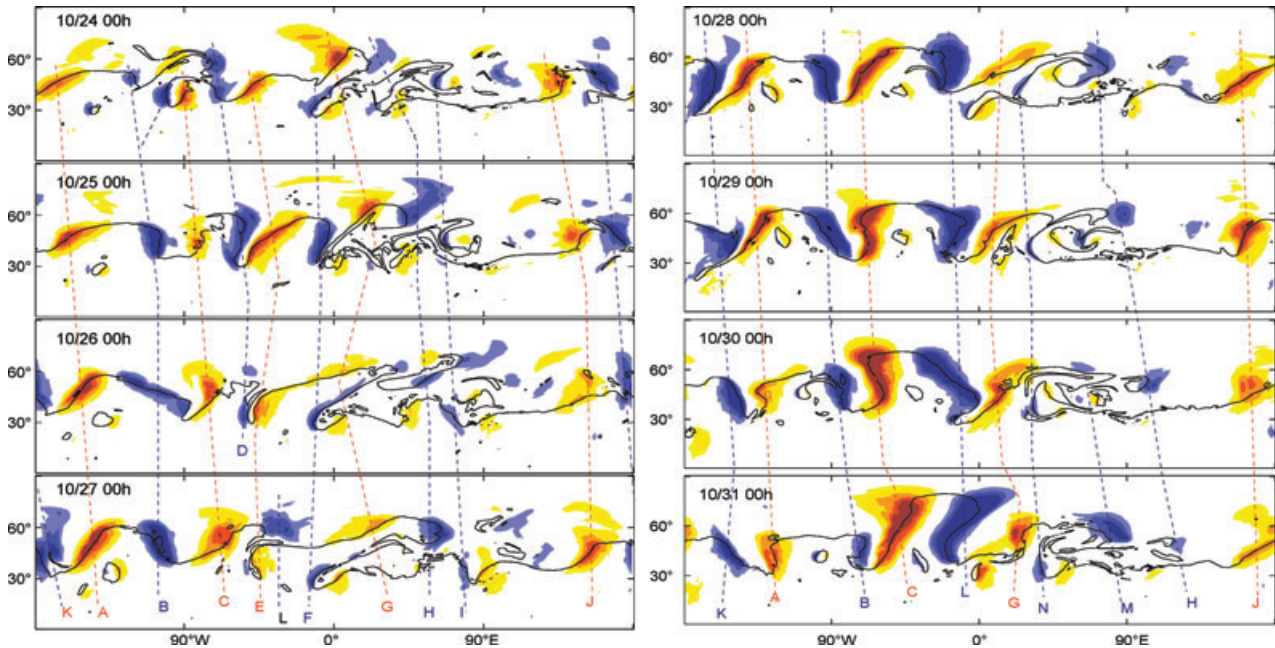


Fig. 12. Representation of the synoptic situation during the short episode from October 24 to 31 on the 330K isentropic surface. Black line: 2 PVU-contour, bluish colours: negative meridional wind  $[(-20, -30, -40, -50) \text{ m}^2 \text{ s}^{-2}]$ , reddish colours: positive meridional wind  $[(20, 30, 40, 50) \text{ m}^2 \text{ s}^{-2}]$ . The blue (negative meridional wind) and red (positive meridional wind) dashed lines denote the position of the extrema in the meridional wind, that are also indicated with the same labels in Fig. 13.

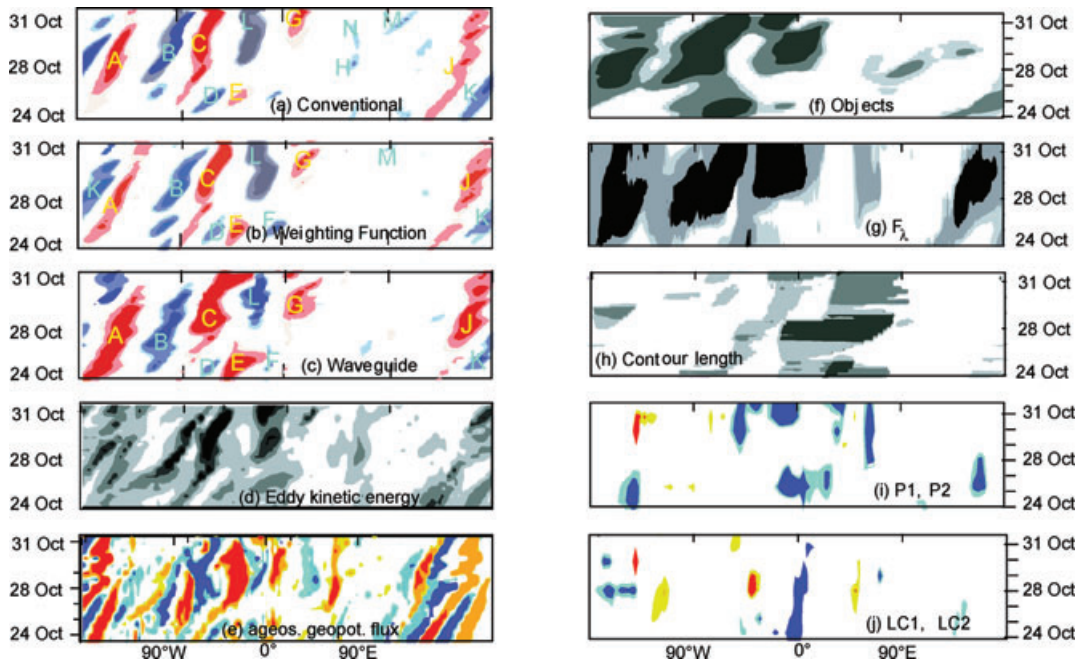


Fig. 13. Period of October 24 to 31 for the Hovmöller diagrams as described in Section 3.

the lowest contour level does not modify this result qualitatively (not shown). Nevertheless, the waveguide Hovmöller diagram does not give the best representation for each single trough or ridge. For example, the feature F is best visible in the weighting function Hovmöller diagram, while the feature M is best rep-

resented in the conventional Hovmöller diagram. The trough-and-ridge Hovmöller diagrams are primarily meant to diagnose a Rossby wave during its quasi-linear propagation stage. It is, therefore, interesting to find out what they indicate during the mature phase with strong Rossby wave breaking. For instance,

let us zoom in on the features H and M, which are associated with large amplitude in Fig. 12. Apparently, these features are barely represented in any of the first three diagrams in Fig. 13. There are mainly two factors responsible for this behaviour. First, substantial parts of the feature H are located outside the range of latitudes contributing to the Hovmöller diagrams. Even the waveguide Hovmöller diagram is apparently not able to capture feature H. At least during its later stages, feature H is associated with a PV-cut-off, and cut-offs are effectively ignored in the waveguide Hovmöller diagram (cf. Martius et al., 2006a). The second factor contributing to the under-representation of H and M is the fact that meridional wind field  $v$  associated with these features is enclosed by steep gradients decaying to zero very quickly—more quickly than for typical other features. As a consequence, the latitudinal average for H and M becomes fairly small despite the fact that these features have large amplitudes locally.

Regarding the eddy kinetic energy diagnostic (fourth panel from top, left column), the different features stand out less clearly than in the trough-and-ridge Hovmöller diagrams discussed before, although they can still be distinguished. Similar as in Section 3.3, the ageostrophic geopotential flux term shows patterns resembling wave packets. But these are overall not consistent with the RWTs identified in panels (a)–(c). Nevertheless this term is useful for deciding whether distinct extrema belong to the same wave train (cf. Chang and Orlanski, 1994). For example, the features C and L indeed belong to the same wave train, as the flux diverges at the eastern part of feature C and converges at the western part of feature L.

In addition, Fig. 13, panels (f) and (g) show two diagnostics which are designed to represent a RWT as a whole entity. Correspondingly, the patterns in panels (f) and (g) do not have a one-to-one relation with the features from previous Hovmöller diagrams; rather, several individual features from the previous diagrams are combined into larger features in (f) and (g). Still, there is a significant amplitude modulation in panels 13 (f) and 13 (g) (which is not sensitively dependent on our choice of the threshold), and some of the RWTs appear to consist of several parts. At first sight this does not seem to be reflected in the synoptic maps of Fig. 12. Yet, closer inspection reveals that it is possible to identify groups of features in Fig. 12. For instance, in the later part of the episode the features J, K and A and features B, C, and L are closer to each other than feature A to feature B. In fact, on October 30 and 31, it is not clear whether A and B still form part of the same RWT. The notion of two distinct wave trains is supported by the fact that the features A and B are not associated with a divergence/convergence dipole in panel (e). The algorithm for our objects allows one to influence to certain extent whether features like A and B are recognized as belonging to the same RWT, or to different (adjacent) ones. This is due to our filter in zonal wavenumber space. The associated choice of parameters allows the user to adapt the diagnostic to the wave numbers of interest. As a way towards a more objective approach

we recommend considering additional diagnostics such as the wave activity flux diagnostic shown in Fig. 13 panel (g). The latter is meant to serve roughly the same purpose, namely to delineate entire RWTs rather than individual troughs and ridges. Indeed, the broad features of Figs. 13 (f) and (g) are similar, and the remaining differences can be taken as an estimate regarding the limit of either method.

During the episode under consideration there is strong Rossby wave breaking between  $\lambda = 0^\circ$  and  $\lambda = 90^\circ\text{E}$ , that is, east of the large-amplitude RWT. This breaking is associated with overturning PV contours in Fig. 12. Figure 13 panels (h)–(j) show how this is reflected in the two diagnostics that quantify Rossby wave breaking. The contour length diagnostic (panel h) indicates wave breaking exactly where the PV contours from Fig. 12 get stretched and turn over. On the other hand, the wave breaking indices representing P1/P2 and LC1/LC2 events [panel (i) and (j)] give a somewhat different picture: they do not coincide very well with the wave breaking derived from the contour length diagnostic [Fig. 13(h)].

This apparent inconsistency can be resolved by considering what actually is measured by the respective diagnostics. The contour length diagnostic provides a Lagrangian measure for the length of PV contours; by construction there is good agreement with the contours in Fig. 12. On the other hand, the breaking index is based on Eulerian fields and measures the amplitude of the meridional wave flux at the time and place when the meridional PV gradient reverses its sign. For instance, there is a large ridge around  $45^\circ\text{W}$  on October 31 (features C and L in Fig. 12) and wave breaking is about to start. There is a large eddy momentum flux in the meridional direction, and the wave breaking index has a correspondingly large value. This is consistent with enhanced P2 values in that region in Fig. 13(i). But at the same time, the 2 PVU contour is not especially long, which is why this event does not show up in the contour length diagnostic in Fig. 13(h). It transpires that the contour length diagnostic tends to diagnose wave breaking during the mature stage of a RWT life cycle, while the wave breaking index of Gabriel and Peters (2008) is more likely to diagnose incipient wave breaking.

#### 4.2. Problematic representation of a specific feature

There is a noteworthy discrepancy in the trough-and-ridge Hovmöller diagrams of Section 3 between September 21 and 27. The weighting-function Hovmöller diagram in Fig. 3 shows an elongated feature around  $90^\circ\text{E}$ , which does not exist in either of the other two diagrams, that is, neither in Fig. 1 nor in Fig. 4(a). In order to resolve this discrepancy, we consider, again, the synoptic evolution on upper tropospheric maps shown in Fig. 14. Throughout the period, a large part of this feature (depicted by the dashed line) lies north of  $60^\circ\text{N}$ , which is outside the averaging window for the conventional Hovmöller diagram. As a consequence, the resulting signal in Fig. 1 becomes very weak. This nicely illustrates the advantage of the weighting function

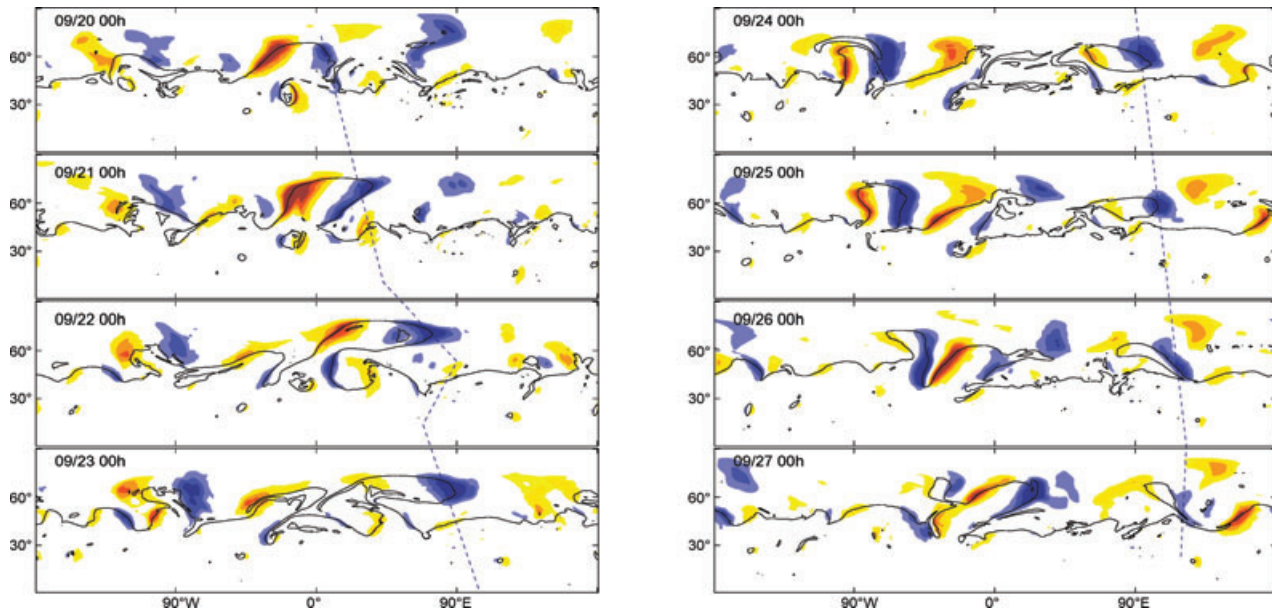


Fig. 14. Representation of the synoptic situation during the short episode from September 20 to 27 on the 330 K isentropic surface. Black line: 2 PVU-contour, bluish colours: negative meridional wind [ $(-20, -30, -40, -50) \text{ m}^2 \text{ s}^{-2}$ ], reddish colours: positive meridional wind [ $(20, 30, 40, 50) \text{ m}^2 \text{ s}^{-2}$ ]. The blue dashed line denotes the position of the trough discussed in the text.

relative to the conventional Hovmöller diagram: instead of being fixed, the latitudinal averaging window is able to adjust to the broad features of the flow.

In principle, the waveguide Hovmöller diagram should do an even better job, as the latitudinal position of the averaging window varies with longitude and is, thus, able to capture even local excursions of the waveguide. Surprisingly, however, the feature in question is not represented in the corresponding Hovmöller diagram in Fig. 4(a). The synoptic maps in Fig. 14 indicate that this feature is associated with a PV-cut-off in the second half of the period and, hence, it is effectively ignored in the waveguide Hovmöller diagram. Furthermore, the strong overturning in the first half of the period brings two parts of the 2 PVU contour lying at the same longitudes. Thus the average of the neighbouring regions of both parts of the 2 PVU contour is taken for the Hovmöller diagram. This reduces the average to a value below the lowest contour level, which is why the feature does not appear in Fig. 4(a).

## 5. Summary and conclusions

In this paper, we have considered several techniques for identifying and characterizing Rossby wave trains. Some of these techniques were developed only recently, while others have been known for a long time. This is the first time that they were considered simultaneously and compared to each other in a systematic manner.

Real atmospheric RWTs constitute a complex and sometimes highly non-linear four-dimensional phenomenon. The investigated techniques reduce this complexity to a two-dimensional

representation in longitude-time-coordinates, that is, Hovmöller diagrams. As a consequence, not all aspects of the Rossby wave train evolution can be represented equally well. Each technique has certain strengths and weaknesses, and they perform differently in the different phases of the evolution of a RWT.

The group of trough-and-ridge Hovmöller diagrams is well suited to diagnose RWTs including full phase information during the propagation phase. In this group, the waveguide Hovmöller diagram of Martius et al. (2006a) generally features RWTs with an apparently larger amplitude than the conventional Hovmöller diagram (Hovmöller 1949) and the weighting function Hovmöller diagram (introduced in this paper). However, this general statement does not apply in every case, and we described a striking counter example in Section 4.2 in which a large-amplitude trough was depicted by the weighting function Hovmöller diagram only.

Split waveguides are notoriously problematic in the framework of Hovmöller diagrams. As a way out it appears possible to adapt the refined versions of the Hovmöller diagram such as to focus on either one of the two waveguides. In the case of the waveguide Hovmöller diagram this may be achieved by choosing an appropriate height level; in the case of the weighting function Hovmöller diagram, the weighting function would have to be modified in order to put emphasis on the latitudes of interest.

Another diagnostic, which has been used frequently in the past, is eddy kinetic energy. It turns out to be less straightforward to identify RWTs in Hovmöller diagrams of the eddy kinetic energy in comparison with trough-and-ridge Hovmöller diagrams. The ageostrophic geopotential flux, which is one of

the terms in the eddy kinetic energy budget, helps to decide whether two extrema in the meridional wind belong to the same wave train. In addition, this and other terms in the eddy kinetic energy budget provide useful and consistent information about the mechanism of trough and ridge formation.

Sometimes one wishes to diagnose a RWT as a complete entity discounting any phase information. Appropriate methods to reach this goal are the RWT objects introduced in this paper, as well as the zonal component of the Plumb (1985) flux  $F_\lambda$ . Both techniques depend on a choice of parameters that determine the amount of spatial smoothing and prior knowledge of the spatial scale of the waves of interest (e.g. in dependence of the season or process) is required.

Two of the methods we considered aim to diagnose aspects during the final stage, which is characterized by Rossby wave breaking. They are rather different in their design and scope. The flux-based breaking index of Gabriel and Peters (2008) primarily measures meridional transfer of zonal momentum during the mature stage of a Rossby wave. On the other hand, the contour length diagnostic of Martius et al. (2006a) tends to maximize during the final stage of a RWT that is characterized by highly non-linear Rossby wave breaking.

Altogether, there is no single 'best' method for identifying and characterizing RWTs. For a given situation or question asked, different techniques are more appropriate than others, and the different diagnostics complement each other. We recommend considering several of these diagnostics in conjunction, in order to obtain a more comprehensive picture than any single technique can provide individually. In the end, the definition of 'Rossby wave train' is made by saying what method is applied for its identification. At first sight this renders the definition objective, but we have seen that different methods focus on different aspects, thus leaving an unavoidable element of subjectivity.

## 6. Acknowledgments

This study is supported by the German Research Foundation (DFG) as part of the research unit PANDOWAE (FOR896). Kaspar Graf from DLR Oberpfaffenhofen kindly provided Fig. 2. We thank the ECMWF for providing IFS Analyses data and A. Gabriel for assistance in running the Rossby wave breaking diagnostics. We thank P. Harr for providing the code of the kinetic energy analysis and supporting the interpretation, as well as E. Chang for valuable discussion and support concerning this analysis.

## References

- Ambaum, M. 2008. Unimodality of Wave Amplitude in the Northern Hemisphere. *J. Atmos. Sci.* **65**, 1077–1086.
- Andrews, D. G. and McIntyre, M. E. 1976. Planetary waves in horizontal and vertical shear: the generalized Eliassen-Palm relation and the mean zonal acceleration. *J. Atmos. Sci.* **33**, 2031–2048.
- Chang, E. K. M. 1993. Downstream development of baroclinic waves as inferred from regression analysis. *J. Atmos. Sci.* **50**, 2038–2050.
- Chang, E. K. M. 1999. Characteristics of wave packets in the upper troposphere. Part II: seasonal and hemispheric variation. *J. Atmos. Sci.* **56**, 1729–1747.
- Chang, E. K. M. 2000. Wave packets and life cycles of troughs in the upper troposphere: examples from the Southern Hemisphere summer season of 1984/85. *Month. Wea. Rev.* **128**, 25–50.
- Chang, E. K. M. 2001. The structure of baroclinic wave packets. *J. Atmos. Sci.* **58**, 1694–1713.
- Chang, E. K. M. and Orlanski, I. 1993. On the Dynamics of a Storm Track. *J. Atmos. Sci.* **50**, 999–1015.
- Chang, E. K. M. and Orlanski, I. 1994. On energy fluxes and group velocity of waves in Baroclinic Flows. *J. Atmos. Sci.* **51**, 3823–3828.
- Chang, E. K. M. and Yu, D. 1999. Characteristics of wave packets in the upper troposphere. Part I: Northern Hemisphere winter. *J. Atmos. Sci.* **56**, 1708–1728.
- Davis, Ch., Brown, B. and Bullock, R. 2006. Object-based verification of precipitation forecasts. Part I: methodology and application to mesoscale rain areas. *Month. Wea. Rev.* **134**, 1772–1784.
- Dritschel, D. G. and McIntyre, M. E. 2008. Multiple jets as PV staircases: the Phillips effect and the resilience of eddy-transport barriers. *J. Atmos. Sci.* **65**, 855–874.
- Eliassen, A. and Palm, E. 1961. On the transfer of energy in stationary mountain waves. *Geophys. Pub.* **22**, 1–23.
- Ertel, H. 1942. Ein neuer hydrodynamischer Wirbelsatz. *Meteorol. Z.* **57**, 227–281.
- Esler, J. G. and Haynes, P. H. 1999. Baroclinic wave breaking and the internal variability of the tropospheric circulation. *J. Atmos. Sci.* **56**, 4014–4031.
- Gabriel, A. and Peters, D. 2008. A diagnostic study of different types of Rossby wave breaking events in the Northern Extratropics. *J. Met. Japan* **86**, 613–631.
- Gibson, A. 2003. Precipitation forecasts for the Central-European Floods, August 2002. *UK-Metoffice unpublished manuscript*.
- Grazzini, F. and van der Grijn, G. 2003. Central European floods during summer 2002. *ECMWF Newsletter* **96**, 18–28.
- Harr, P. A. and Dea, J. M. 2009. Downstream development associated with the extratropical transition of tropical cyclones over the western north pacific. *Month. Wea. Rev.* **137**, 1295–1319.
- Hoskins, B. and Berrisford, P. 1988. A potential vorticity view of the storm of 15–16 October 1987. *Weather* **43**, 122–129.
- Hoskins, B. and Valdes, P. J. 1990. On the existence of storm-tracks. *J. Atmos. Sci.* **47**, 1854–1864.
- Hovmöller, E. 1949. The trough- and ridge diagram. *Tellus* **2**, 62–66.
- Jones, S., Harr, P., Abraham, J., Bosart, L. F., Evans, J. L. and co-authors. 2003. The extratropical transition of tropical cyclones: forecast challenges, current understanding, and future directions. *Wea. Forecast.* **18**, 1052–1092.
- Lee, X. 1997. Gravity waves in a forest: a linear analysis. *J. Atm. Sci.* **54**, 1726–1738.
- Lee, S. and Held, I. 1993. Baroclinic Wave Packets in Models and Observations. *J. Atmos. Sci.* **50**, 1413–1428.
- Madden, R. A. 2007. Large-scale, free Rossby waves in the atmosphere – an update. *Tellus* **59**, 571–590.
- Martius, O., Schwierz, C. and Davies, H. 2006. A Refined Hovmöller Diagram. *Tellus* **58A**, 221–226.

- Martius, O., Zenklusen, E., Schwierz, C. and Davies, H. 2006. Episodes of Alpine heavy precipitation with an overlying elongated stratospheric intrusion: a climatology. *Int. J. Climatol.* **26**, 1149–1164.
- Martius, O., Schwierz, C. and Davies, H. 2007. Breaking waves at the Tropopause in the wintertime Northern Hemisphere: climatological analyses of the orientation and the theoretical LC1/2 classification. *J. Atmos. Sci.* **64**, 2576–2592.
- Martius, O., Schwierz, C. and Davies, H. 2008. Far-Upstream Precursors of Heavy Precipitation Events on the Alpine South-Side. *Q. J. R. Met. Soc.* **34**, 417–428.
- Martius, O., Schwierz, C. and Davies, H. 2010. Tropopause-Level Waveguides. *J. Atmos. Sci.* **67**, 866–879.
- McIntyre, M. and Palmer, T. 1985. A Note on the General Concept of Wave Breaking for Rossby and Gravity Waves. *Pa. Geoph.* **123**, 964–975.
- McIntyre, M. E. and Palmer, T. N. 1983. Breaking planetary waves in the stratosphere. *Nature* **305**, 593–600.
- Nakamura, H. and Plumb, R. A. 1994. The effects of flow asymmetry on the direction of Rossby-wave breaking. *J. Atmos. Sci.* **51**, 2031–2045.
- Nishii, K. and Nakamura, H. 2004. Tropospheric influence on the diminished Antarctic ozone hole in September 2002. *Geophys. Res. Lett.* **31**, DOI:10.1029/2004GL019532.
- Orlanski, I. and Katzfey, J. 1991. The life cycle of a cyclone wave in the southern hemisphere. Part I: Eddy energy budget. *J. Atmos. Sci.* **48**, 1972–1998.
- Orlanski, I. and Sheldon, J. 1995. Stages in the energetics of baroclinic systems. *Tellus* **47A**, 605–628.
- Palmén, E. H. and Newton, Ch. W. 1969. *Atmospheric Circulation Systems*. Academic Press, New York.
- Peters, D., Vargin, P. and Kornich, H. 2007. A study of the zonally asymmetric tropospheric forcing of the austral vortex splitting during September 2002. *Tellus* **59A**, 384–394.
- Peters, D. and Waugh, D. W. 1996. Influence of barotropic shear on the poleward advection of upper-tropospheric air. *J. Atmos. Sci.* **53**, 3013–3031.
- Peters, D. and Waugh, D. W. 2003. Rossby wave breaking in the Southern Hemisphere wintertime upper troposphere. *Month. Wea. Rev.* **131**, 2623–2634.
- Plumb, R. A. 1985. On the three-dimensional propagation of stationary waves. *J. Atmos. Sci.* **42**, 217–229.
- Postel, G. and Hitchman, M. 1999. A climatology of Rossby wave breaking along the subtropical tropopause. *J. Atmos. Sci.* **56**, 359–373.
- Rossby, C.-G. 1945. On the propagation of frequencies and energy in certain types of oceanic and atmospheric waves. *J. Meteor.* **2**, 187–204.
- Schwierz, C., Dirren, S. and Davies, H. 2004. Forced waves on a zonally aligned jet stream. *J. Atmos. Sci.* **61**, 73–87.
- Scinocca, J. F. and Shepherd, T. G. 1992. Nonlinear wave-activity conservation laws and Hamiltonian Structure for the two-dimensional Anelastic Equations. *J. Atmos. Sci.* **49**, 5–27.
- Shapiro, M. and Thorpe, A. 2004. THORPEX International Science Plan. *WMO/TD* **1246**.
- Takaya, K. and Nakamura, H. 2001. A formulation of a phase-independent wave-activity flux for stationary and migratory quasi-geostrophic eddies on a zonally varying basic flow. *J. Atmos. Sci.* **58**, 608–627.
- Wernli, H., Paulat, M., Hagen, M. and Frei, Ch. 2008. SAL - a novel quality measure for the verification of quantitative precipitation forecasts. *Month. Wea. Rev.* **136**, 4470–4487.
- Annual Bulletin on the Climate in WMO Region VI - Europe and Middle East, 2008. The Network of European Meteorological Services and World Meteorological Organization and Deutscher Wetterdienst. [http://www.dwd.de/bvbw/generator/DWDWWW/Content/Oeffentlichkeit/KU/KU2/KU23/ravi\\_bulletin/bulletin\\_2008\\_templateId=raw.property=publicationFile.pdf/bulletin\\_2008.pdf](http://www.dwd.de/bvbw/generator/DWDWWW/Content/Oeffentlichkeit/KU/KU2/KU23/ravi_bulletin/bulletin_2008_templateId=raw.property=publicationFile.pdf/bulletin_2008.pdf).
- Zimin, A., Szunyogh, I., Patil, D. and Ott, E. 2003. Extracting envelopes of Rossby Wave Packets. *Month. Wea. Rev.* **131**, 1011–1017.